Physica E 140 (2022) 115142

Contents lists available at ScienceDirect

Physica E: Low-dimensional Systems and Nanostructures

journal homepage: www.elsevier.com/locate/physe

Broadband terahertz metamaterial absorber and modulator based on hybrid graphene-gold pattern

Yisong Lv [a], Wen Liu [a], Jinping Tian [a,b,*], Rongcao Yang [a]

[a] College of Physics and Electronics Engineering, Shanxi University, Taiyuan, 030006, PR China
[b] Computer Center, School of Modern Education Technology, Shanxi University, Taiyuan, 030006, PR China

ARTICLE INFO

Keywords:
Metamaterial absorber
Dynamical tunability
Broadband
Modulator

ABSTRACT

We have numerically demonstrated a tunable broadband metamaterial absorber (MA) by introducing a graphene pattern and a gold disk, of which the bandwidth is up to 3.4 THz. When the chemical potential of graphene changes from 0 eV to 0.5 eV, the proposed MA structure can also be used as a modulator with the minimum and maximum modulate depth being about 69.5% and 92.5%, respectively. By tuning the relaxation time of the graphene from 0.1 ps to 0.5 ps, several obvious absorption peaks will occur in the broad and flat absorption band, which will deteriorate the broadband absorption characteristics and make it show a trend of multi-band absorption characteristics. To further increase the absorption bandwidth, a new graphene pattern and an additional gold disk are added into the proposed MA structure to form a new type of MA structure. Simulation result shows that the newly designed MA structure can achieve a wider absorption bandwidth of more than 4.0 THz. Meanwhile, it still has the performance of excellent modulation characteristic, polarization insensitive and wide tolerance of incident angles. All these optimal characteristics of the proposed MA structures will undoubtedly benefit the use of metamaterial absorber, high speed communication, terahertz detection devices, optoelectronic devices and so on.

1. Introduction

Many of the electromagnetic properties possessed by metamaterials which do not exist in nature, are superior to those natural materials, such as negative refraction [1,2] sensing [3,4], detection [5], perfect lens [6,7] and so on. Therefore, electromagnetic metamaterial equipment are widely used in various light bands, such as microwave [8,9], millimeter wave [10], terahertz (THz) [11], near-infrared and visible frequencies [12,13], and so on. Among the extensive research content, metamaterial absorbers (MA) have been a hot spot in recent years. For example, Tao et al. proposed a THz MA by bilayer metal resonant ring in 2008 [14], and the structure can achieve maximum absorption by independently adjusting the electrical permittivity and magnetic permeability. In Ref. [15], researchers designed a type of MA to achieve multi-band absorbing which consists of three multi-gap split-ring resonators with different radii and ring widths. In Ref. [16], four narrow absorption bands in THz frequency domain are demonstrated in a MA consisted of three metallic layers. In Ref. [17], MA composed of double-layer copper square ring is designed, and an absorption rate of more than 93% can be achieved. And a similar copper ring array structured MA has also been proposed and perfect three-band absorption in the microwave frequency band is obtained [18]. In Ref. [19] in 2018, an ultra-broadband infrared perfect absorber was experimentally demonstrated based on the coupled plasmonic-photonic micro-cavities, which was fabricated on the template of a non-close-packed colloidal crystal.

A lot of research works have confirmed that most MAs are due to the strong surface plasmon resonance (SPR), which is the result of coupling between the incident light and the free electrons at the interface between dielectric medium and metal. The SPR produced at the interface can convert the incident energy into confined surface plasmonic polaritons (SPP) and then capture or dissipate it in the structure. Therefore, the electric resonance and magnetic resonance coming from propagating surface plasmon resonance (PSPR) and localized surface plasmon resonance (LSPR) together with the Fabry-Perot (FP) resonance are all the issues that will dominate the absorption [20]. However, the performance of metal-based MAs will be fixed due to the stable conductivity of the metal and the unalterable geometry structure after fabrication, which seriously hinders their practical application. Therefore, the application of MA with adjustable conductivity or with dynamically

* Corresponding author. College of Physics and Electronics Engineering, Shanxi University, Taiyuan, 030006, PR China.
E-mail address: tianjp@sxu.edu.cn (J. Tian).

https://doi.org/10.1016/j.physe.2022.115142
Received 30 June 2021; Received in revised form 3 January 2022; Accepted 8 January 2022
Available online 11 February 2022

tunable functions is strongly desired. Interestingly, many functionally tunable materials such as vanadium dioxide (VO_2), molybdenum disulfide (MoS_2), black phosphorus (BP) and graphene have been proposed in the design of MAs in recent years. For example, in Ref. [21], researchers proposed a sandwich nanostructured MA composed of a VO_2 film, a SiO_2 layer and a metal cross array, of which the absorption can be increased from 20% to 95% by tuning the conductivity of VO_2. In research work [22], a polarization-independent and wide-angle MoS_2--based absorber is proposed, and the broadband absorber can be changed to be multiband absorber by changing the thickness of dielectric substrate. In Ref. [23], a MA composed of a monolayer black phosphorus (BP) is proposed, which can achieve perfect absorption under the condition of critical coupling. Among the novel functional materials mentioned above, graphene is composed of a single layer of honeycomb carbon atoms, which can be fabricated through quite mature processing and manufacturing technologies. Graphene has high carrier mobility at room temperature and is widely used in optical, electrical and thermal area. Graphene can also support SPR when it is applied to construct optoelectronic devices in terahertz, near infrared, and microwave frequency bands. Among the reported literatures, graphene-based THz MAs have attracted increasing numbers of researchers' concern in developing MA devices with better performance. It is known that the absorption of a single graphene sheet is only about 2.3% [24,25], therefore, in order to enhance the absorption of graphene, a large number of different graphene patterns are designed to excite electromagnetic resonances based on SPPs. For example, in Ref. [26], the authors constructed a perfect MA using graphene micro-ribbons and verified the accuracy of the results with the F-P cavity model. An MA structure based on graphene strip arrays or disk arrays was designed and perfect dual-band absorption was achieved [27], and the dual-band absorption was also achieved in a type of MA composed of both graphene disk and strip structure [28]. In Ref. [29], the authors achieved perfect absorption of dual-band and tri-band absorption by using different widths of graphene strips, but the asymmetry of the MA structure makes it very sensitive to the polarization angle. Moreover, a four-band ideal absorber using monolayer graphene are proposed based on critical coupling and guided resonance [30], and other types of multi-band perfect absorbers consist of different graphene patterns were designed in Refs. [31–34]. Apart from those single-band and multi-band graphene based MAs, in Ref. [35], an ultra-broadband multilayers graphene based MA was proposed, of which asymmetric graphene patterns with different chemical potential were applied to generate high-order plasmon modes, and with the help of destructive interference between the quadrapolar modes and the dipolar ones, ultra-broadband absorption was achieved. In research work [36], a periodically sinusoidally-patterned graphene pattern was used to realize the broadband absorption. Meanwhile, in order to obtain more tunability, hybrid materials with different properties have been applied to realize multifunctional tunable MA. For example, a switchable broadband THz spatial modulator composed of graphene and VO_2 was proposed [37], which can achieve modulation depth (MD) of 84.8% under absorption mode and of 59.2% under transmission mode. A bifunctional MA composed of graphene and VO_2 was also been proposed to achieve broadband or narrowband absorption [38] by adjusting the relaxation time of graphene from 0.1 ps to 1 ps. However, many reported MAs have the disadvantage of narrower absorption bandwidth. Therefore, broadband tunable perfect MAs using graphene and other functional materials are still a current research hot spot, and it is necessary to design more tunable broadband THz MAs with more excellent performance based on graphene and other tunable materials as well as their combinations.

Generally, broadband absorption can be obtained through stacking multilayered structure or constructing patterns with different sizes in a same metasurface. In this work, a compound MA structure is designed, of which the top layer is a hybrid structure of graphene pattern and gold disk, the middle spacer layer is polyethylene cyclic olefin copolymer (Topas), and the bottom layer is a gold ground plate. It is found that

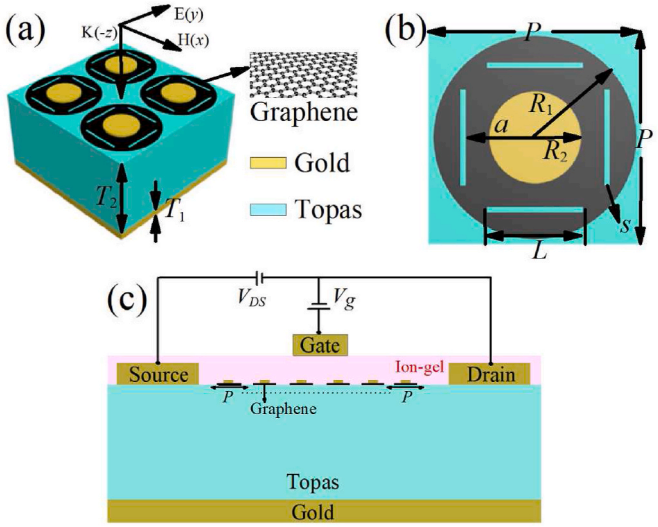

Fig. 1. (a) 3D schematic diagram of the proposed broadband MA structure, (b) top view of a unit cell of the proposed MA structure, (c) schematic view of top gate structure tuning graphene chemical potential. The incident electromagnetic wave, material and parameters are also shown in the figure.

cutting out different numbers of slits (from zero to four) in the graphene will lead to the different degrees of absorption effect, and the broadband absorption can be achieved by cutting out four symmetrically distributed slits. As a result, based on the enhanced field confinement around the nano-slits and the field hybridization between different parts of the structure, broadband absorption was well achieved using a type of simple structure based on the periodically patterned graphene and gold disk. When the chemical potential of graphene was adjusted from 0 eV to 0.5 eV, besides the narrowing absorption bandwidth, the proposed MA structure can also be used as a modulator with minimum and maximum MD of 69.5% and 92.7%, respectively. At the same time, when the relaxation time of graphene is adjusted from 0.1 ps to 0.5 ps, together with the decrease of absorption bandwidth, the proposed MA structure can even realize the transition from broadband absorption to multi-band absorption. In addition, it is found that by adding a new combination of graphene pattern and gold disk to the top layer of the MA structure, the absorption bandwidth can be further broadened to near 4.0 THz with the minimum and maximum MD of 70.57% and 91.5%, respectively. Meanwhile, properties of dynamically adjustability, wide-angle incidence and polarization insensitivity are also achieved. In order to carry out the research, the electromagnetic simulation software CST based on finite integration technology is adopted. Periodic boundary condition is set along the *x*-axis and *y*-axis, while the *z*-axis is set as open (add space). Owing to the excellent absorption performance of the proposed MA structure, it not only has potential application value in providing ideas for the design of more broadband THz MA, but also in the area of high-speed intelligent detection devices of THz and optoelectronic devices.

2. Structure and method

The 3D schematic diagram of the proposed tunable broadband MA structure is shown in Fig. 1. In the THz frequency range, the permittivity of Topas is $\varepsilon_d = 2.35$ [36,39,40], the conductivity of gold is $\sigma_{A_u} = 4.561 \times 10^7 S/m$ [41]. To be noted is that although dielectric losses are helpful to enhance the absorption in some MAs [42], we neglect the losses of dielectric medium Topas in this paper, because we have found during the design process that its influence on the overall absorption performance is not very clear. The optimized geometric parameters are set as $P = 8\mu m, T_1 = 0.2\mu m, T_2 = 8\mu m, R_1 = 3.8\mu m, R_2 = 1.7\mu m, a = 2.7\mu m, L = 3.6\mu m, s = 0.2\mu m$, and whose meanings are shown in Fig. 1 (a) and (b). Although the optimization of parameters can be achieved by

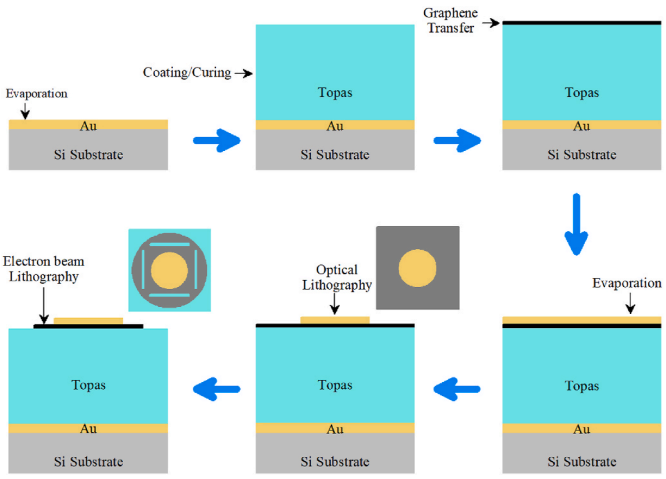

Fig. 2. Possible fabrication process/step for the realization of the proposed metamaterial absorber.

various methods, such as convolutional neural network, deep learning model [43], for simplicity, the built-in tool of CST was applied to the optimized geometric parameters in this paper.

The proposed structure can be fabricated with the state-of-art nanofabrication technology, as shown in Fig. 2. At first, gold can be grown by using electron beam evaporation or thermal evaporation system onto a thick enough silicon substrate. Then a thick layer of Topas spacer layer can be formed by the processes of spin-coating and curing on the gold ground. At the same time, a large scale single-layer graphene sheet has been grown on the copper by the quite mature chemical vapor deposition method. Therefore, the second step is to transfer the graphene sheet onto the Topas layer with Raman measurements being used to ensure that the single-layer graphene is produced. At third, a thin gold layer can be deposited on the top by the same method. Finally, the gold disk can be fabricated with conventional optical lithography technology, and the complex graphene pattern can be obtained by electron beam lithography, reactive ion etching or oxygen plasma etching systems through removing the redundant region [44–47]. In addition, in order to adjust the chemical potential dynamically by applying an external gate voltage, a layer of transparent ion-gel can be further coated onto the whole structure with gold bars evaporated at specific locations acting as electrodes of source, drain and gate voltages, as shown in Fig. 1(c).

During simulation, graphene is modeled as a zero-thickness 2D material, of which $\sigma_g = \sigma_{intra} + \sigma_{inter}$ is its surface conductivity, and it can be described by the Kubo formula [48–50].

$$\sigma_{\text{intra}}(\omega,\mu_c,\Gamma,T) = \frac{ie^2K_BT}{\pi\hbar^2(\omega+i2\Gamma)}\left[\frac{\mu_c}{K_BT}+2ln\left(e^{-\frac{\mu_c}{K_BT}}+1\right)\right] \quad (1)$$

$$\sigma_{\text{inter}}(\omega,\mu_c,\Gamma,T) = \frac{ie^2}{4\pi\hbar}ln\left(\frac{2|\mu_c|-(\omega+i2\Gamma)\hbar}{2|\mu_c|+(\omega+i2\Gamma)\hbar}\right) \quad (2)$$

where ω is the radian frequency, μ_c is the chemical potential of graphene, $T = 300$K is the temperature, $\Gamma = (2\tau)^{-1}$ is the phenomenological scattering rate and τ is the relaxation time, which is set as 0.1 ps at the initial stage. Besides, e, $\hbar$ and K_B represent the charge of an electron, the reduced Plank's constant, and the Boltzmann's constant, respectively. The conductivity of graphene can be dynamically adjusted by changing the chemical potential μ_c, which can be controlled by adding an electrode after covering a layer of ionic gel on the top of the structure without affecting the overall absorption performance. To dynamically adjusting the chemical potential of the graphene, schematic diagram shown in Fig. 1(c) is widely applied [51–55]. In terms of [51], the ion-gel layer can be chemically prepared to yield a high capacitance of $C = 2.45\mu F/cm^2$ with low absorption. Then the chemical potential could

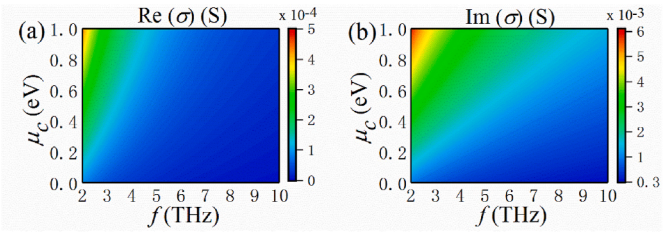

Fig. 3. (a) Real and (b) imaginary part of the surface conductivity of the graphene as functions of the working frequencies and the chemical potentials.

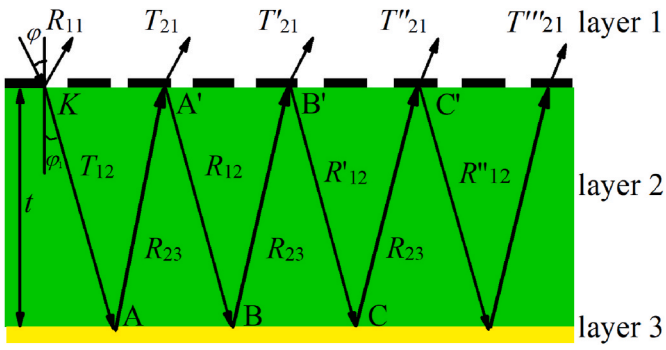

Fig. 4. Simplified principle diagram of the multiple reflection interference theory (MRIT) for a classic three-layer MA structure.

be effectively tuned from 0.2 to 0.8 eV by applying a top gate bias voltage according to $\mu_c = \hbar v_F\sqrt{\pi n}$, where $v_F = 10^6$ m/s is the Fermi velocity, and the carrier density $n = CV_{DG}/e$, where V_{DG} is the gate bias voltage. Similarly, one can also obtain the relationship between the chemical potential of graphene and the gate voltage in terms Refs. [52–55], and so on. From Fig. 3(a) and (b), one can clearly see that both of the real and imaginary parts of the graphene conductivity increase with the increase of the chemical potential for a fixed frequency within the frequency range of 2–10 THz.

In this paper, the absorption rate of the proposed MA structure can be expressed by $A = 1 - |r|^2 - |t|^2$, where $r = S_{11}$ and $t = S_{21}$, which can be obtained directly from numerical simulation. Owing to the fact that the thickness of the bottom gold plate is larger than its largest skin depth, the transmission is zero ($S_{21} = 0$) and thus we have $A = 1 - |r|^2$. In addition, it is well-known that perfect absorption occurs when the impedance of the MA structure matches with that of the free space. The normalized effective surface impedance of an MA with a gold ground plate can be expressed as

$$Z(f) = \sqrt{\frac{(1+S_{11})^2 - S_{21}^2}{(1-S_{11})^2 - S_{21}^2}} = \frac{1+S_{11}}{1-S_{11}} \quad (3)$$

When S_{11} and S_{21} are both zero, the normalized surface impedance $Z(f) = 1$, which means that the impedance matching condition between the free-space and the MA is achieved, thus perfect absorption can be obtained. Meanwhile, multiple reflection interference theory (MRIT) is also often used to verify the simulation results, which is proposed firstly by H. T. Chen in 2010 [56]. The principle diagram of MRIT is shown in Fig. 4. After multi times of reflection and transmission at the interfaces between layer 1 and layer 2, and between layer 2 and layer 3, the overall reflection coefficient can be expressed as:

$$r = R_{11} - \frac{T_{12}T_{21}\exp(2i\beta d)}{1+R_{12}\exp(2i\beta d)} \quad (4)$$

where φ is the incident angle and φ_1 is the corresponding refractive angle. The reflection and transmission coefficients at different interfaces

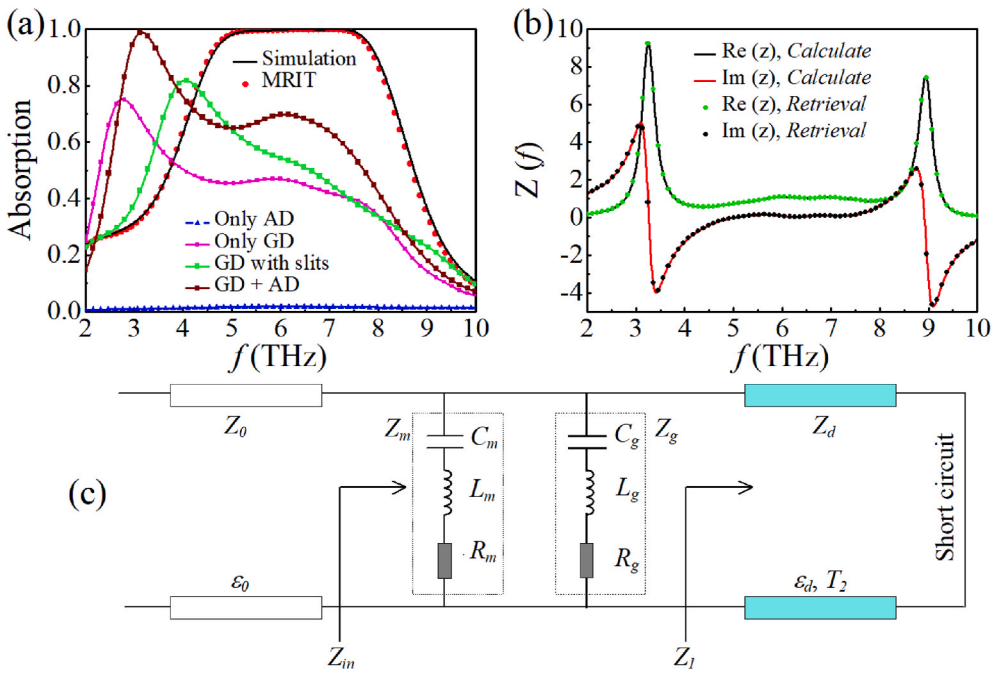

Fig. 5. (a) The black solid curve is the absorption spectrum of the proposed MA structure and the red dotted curve is the result calculated by MRIT, the blue, pink, green and wine curves are respectively the absorption spectrum for the case of having only gold disk (AD), only graphene disk (GD), graphene disk with four slits and both gold disk and graphene disk. (b) The black and red solid curves are the real and imaginary part of the calculated normalized surface impedance directly using Eq.(3), while the green and black dotted curves are the retrieval results obtained according to the reported references. (c) Transmission line and equivalent circuit models for the proposed metamaterial absorber.

and along different directions are $R_{11} = r_{11}e^{i\theta_{11}}$, $T_{12} = t_{12}e^{i\varphi_{12}}$ $T_{21} = t_{21}e^{i\varphi_{21}}$, $R_{12} = r_{12}e^{i\theta_{22}}$ and $R_{23} = -1$, respectively. The phase shift in the Topas layer can be represented by $\beta = \sqrt{\varepsilon_d}k_0 d$, where k_0 is the wave number in the free space, and $d = t/\cos(\varphi_1)$. When the incident angle φ is zero, namely, for the normally propagating incident light, $d = t$ is satisfied.

3. Simulation and discussion

First, by selecting the chemical potential as 0.5 eV, we simulate the absorption spectrum of the proposed MA and its decomposed structure with the parameters given in the above section, and the simulation results are shown in Fig. 5(a). The black solid curve is the absorption spectrum of the proposed MA, and the blue, pink, green and wine curves are the absorption spectrum for the case of having only gold disk (AD), only graphene disk (GD), graphene disk with four slits and both gold disk and graphene disk, respectively. It can be found that the absorption is very bad if only gold disk is used because the resonance is not effectively excited at this time and the incident light are reflected, as shown by the blue curve. If only graphene disk is used, as shown by the pink curve, the absorption performance is improved compared to the case of gold disk, which means that resonance with a certain intensity occurs, leading to the weaker broadband absorption with an absorption peak located at about 2.77 THz. As further attempts, cases of graphene disk with four slits and combining gold disk and graphene disk are considered, as shown by the green and wine curves. It is clear that cutting four slits is helpful to increase to absorption intensity, but reduces the bandwidth. However, the combination of gold disk and graphene disk can greatly increase the absorption intensity without significantly changing the bandwidth, and under this circumstance, a near unity absorption peak occurs at about 3.24 THz together with the clearly enhanced absorption at high frequencies. It is these four simple cases that inspired us propose the MA structure shown in Fig. 1, namely, combining the graphene disk with four slits and the gold disk together to simultaneously increase the overall absorption intensity and broaden the bandwidth. One can find from the black curve that broadband nearly perfect absorption is indeed achieved and the absorption is larger than 90% within the frequency range from 4.6 THz to 8 THz with the absorption bandwidth being close to 3.4 THz. In brief, we can conclude that the perfect broadband absorption is achieved by making the full use of the hybridization effect between the SPR excited on the graphene disk and gold disk, while the four slits on graphene can further enhance the hybridization and coupling, leading to the broadband nearly perfect absorption. In addition, due to the coupling interaction, when the broadband absorption spectrum is formed, the low frequency resonance shows an obvious blueshift. Next, we have analytically calculated the absorption using MRIT, as shown by the red dotted curve, and it is obvious that the MRIT result can maintain good consistency with the simulation result, which also verifies the accuracy of our study. Meanwhile, this also indicates that the top combined layer, the spacer layer and the gold ground layer can form a Fabry-Perot (FP) resonator. The multiple reflection will occur in the FP resonator, and the reflected waves will interfere destructively with each other at the top layer, enhancing the overall absorption performance. Fig. 5(b) represents the calculated normalized impedance of the proposed MA. The black and red solid curves represent the real and imaginary part of the impedance calculated directly through Eq. (3), and the green and black dotted curves are obtained by parameter retrieval theory according to Refs. [57,58], and it is obvious that the two results agree well with each other. When the real part of the normalized impedance is close to 1 and the imaginary part is close to 0 in the considered frequency band, nearly perfect impedance matching condition is achieved, and nearly perfect absorption is obtained. One can really find from Fig. 5(b) that the impedance matching condition is well satisfied within the frequency range of about 4.6–8 THz, which means the nearly perfect absorption and is in accordance with the result shown in Fig. 5(a). Fig. 5(c) is the equivalent circuit model of the proposed MA, where the bottom gold layer can be considered as a short circuit and $Z_1 = jZ_d\tan(\beta_d T_2)$ is impedance of Topas layer with thickness T_2, β_d is the propagation constant of the propagating light waves in the Topas layer and $Z_d = Z_0/\sqrt{\varepsilon_d}$ with Z_0 being the free space impedance. The overall input impedance of the proposed MA can be seen as the parallel connection. Z_1, Z_m and Z_g, namely

$$\frac{1}{Z_{in}} = \frac{1}{Z_1} + \frac{1}{Z_g} + \frac{1}{Z_m} \tag{5}$$

where $Z_g = R_g + j\omega L_g + 1/j\omega C_g$ and $Z_m = R_m + j\omega L_m + 1/j\omega C_m$ are respectively the impedance of gold disk and graphene pattern, which

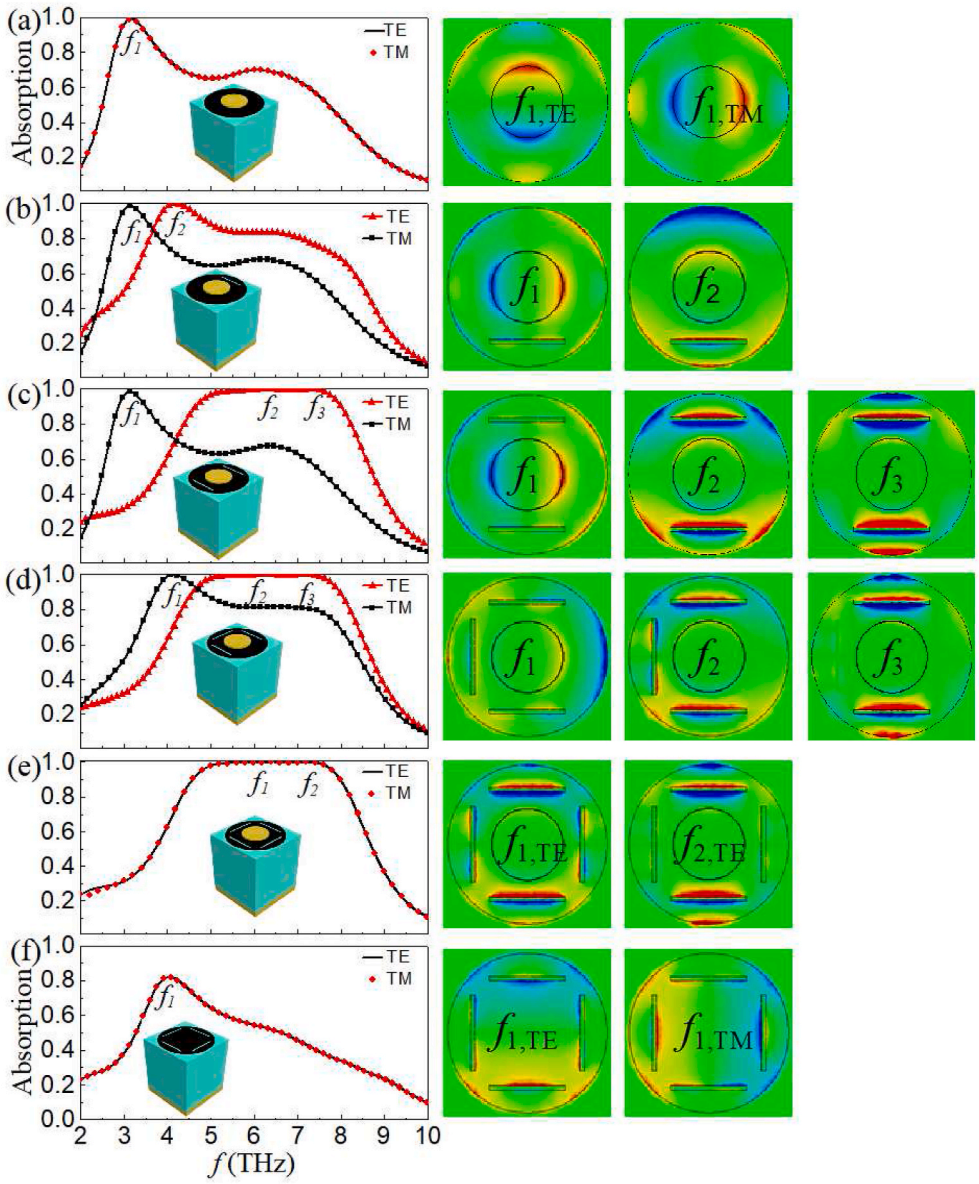

Fig. 6. Absorption spectra when (a) no slit, (b) one slit, (c) two slits, (d) three slits, and (e) four slits are cut out in the graphene under normally incident TE and TM wave, while (f) is the case of no gold disk but with four slits in the graphene. Inset is the corresponding MA structure and the color map is the corresponding electric field distribution of *Ez* at the frequency where the absorption is maximum.

can be retrieved by numerical simulation and analytical calculation. The resistance, the inductance and the capacitance are related to the inherent characteristics of gold disk and graphene pattern as well as the dimensions of the different parts of the proposed MA. Then the corresponding absorption of the proposed MA can be written as:

$$A = 1 - |r'|^2 = 1 - |S_{11}|^2 = 1 - \left|\frac{Re(Z_{in}) - Z_0}{Re(Z_{in}) + Z_0}\right|^2 \tag{6}$$

According to Ref. [59], the imaginary part of the input impedance must be equal to zero at the resonant frequencies where the absorption is maximum, and the resonant frequency can be described by $f = 1/2\pi\sqrt{LC}$, where L and C are respectively the total equivalent inductance and capacitance. Therefore, the absorption performance of the proposed MA is mainly determined by the relevant parameters of the graphene pattern and the gold disk.

Then, we discuss the mechanism of the broadband absorption property as well as the realizing process of the broadband absorption. At the beginning, let us consider the case when the top layer is composed of stacked gold disk and graphene disk, and the simulation result is shown in Fig. 6(a). It is clear that due to the symmetry of the structure, for the normally incident TE (the electric field component is along *y*-direction) and TM (the magnetic field component is along *y*-direction) light, the two absorption spectral lines are coincided with each other, however, the effect of broadband absorption is not well achieved. At the absorption peak and along the direction of the incident electric field, stronger dipolar resonance can be excited on the graphene disk at first for both TE and TM incident light due to the excitation of SPPs at the ends of graphene disk. Next, the confined electric field from SPR on the graphene disk will further excite the SPPs at the edges of the gold disk through near field coupling, forming the dipole distribution. And then hybridization will be produced between the SPR on the gold disk and the SPR on the graphene disk. It is this hybridization that results in the rearrangement of the distribution of the electric fields along the graphene disk. As a result, the in-phase hybridization leads to the low frequency near unity absorption, while the out-of-phase hybridization clearly enhanced the absorption at high frequencies. Meanwhile, it also indicates that the

strong absorption at low frequency is mainly determined by the graphene disk, and at the higher frequencies, SPRs on gold disk together with its coupling interaction with those on the graphene disk play a vital role. It is obvious that either the dipolar resonance excited at the edges of gold disk or the multipole resonance along the edges of graphene is LSPR, and it is the LSPR [20,42] that confines the electric field of the incident light to the top layer of the proposed MA, dominating the absorption of a larger part of the field energy. Meanwhile, due to the thicker Topas spacer layer, coupling between the top layer and the bottom gold layer is relatively weak. Therefore, magnetic resonance excited in the spacer layer is also very weak, and simulation showed that weaker magnetic field only distributed around the top layer. In fact, the perfectly consistent analytical result from MRIT can also prove this, as shown in Fig. 5(a), because one of the prerequisites for using MRIT is the very weak coupling between the upper and lower layers of the designed MA structure. In addition, simulation results also showed that PSPR excited at the interface of the Topas layer and the bottom gold layer was also weaker because the wave vector of diffraction waves coming from the top layer did not well match that of SPR along this interface. Therefore, the following discussion will mainly focus on the upper layer. Nevertheless, both of the very weak magnetic fields and the PSPR still have some slight effects on the overall absorption enhancement.

Inspired by Ref. [34], introducing a nano-slit in the graphene disk can increase the number of absorption peaks, and then the superposition of nearby absorption peaks can be used to achieve broadband absorption. Therefore, to achieve broadband absorption based in the proposed MA, at first, we cut out one slit in the graphene along x-direction, where the length and width of the slit are $L = 3.6\mu$m and s $= 0.2\mu$m, respectively, and the simulation result is shown in Fig. 6(b). One can find that the broadband absorption characteristics have been greatly improved for TE light except some blueshift in the absorption peak. And at this time, due to the existence of nano-slit on the graphene, the distribution of the electric fields was clearly changed. Not only the electric fields confined on the graphene edges are strongly enhanced, but also a part of electric fields are confined around the nano-slit. Therefore, with the blue shift of the low frequency absorption peak, the overall absorption performance is also largely enhanced, and the frequency range of absorption rate larger than 80% is up to about 4.85–7.04 THz. For TM light, the change is not clear compared with Fig. 6(a). According to this, as shown in Fig. 6(c), two parallel slits with the same size are cut out from the graphene on both sides of the gold disk along x-direction. As a result and it is interesting that the broadband near unity absorption characteristic for TE light is indeed realized. It can be seen that the frequency range of absorption rate exceeding 90% is extended to about 4.6–8.0 THz, and the bandwidth is up to 3.4 THz. According to electric field distribution corresponding to the two absorption peaks in the broad absorption frequency band, the two slits on the graphene confine a lot of electric fields due to the excited plasmonic resonance along the edges of the slits. In addition, there are also some electric fields that are strongly confined around the edge of the graphene disk. However, due to the hybridization and coupling interaction of SPPs among the gold disk, the graphene slits and the graphene disk itself, the electric field distribution along the gold disk is suppressed. Nevertheless, the gold disk still plays a vital role to the formation of broadband absorption. In brief, the strong absorption at low frequency side is mainly dominated by the electric fields confined along the graphene disk. With the increase of frequency, the effect of graphene slits increases gradually. Due to the hybridization of SPRs, the electric field distribution changes significantly, which dramatically enhanced the absorption at the high frequency, forming the broadband absorption. However, for TM light, the broadband absorption is still not ideal. To improve the broadband absorption characteristic of TM light, one more slit is cut out along y-direction. As shown in Fig. 6(d), the absorption characteristic of TM light indeed have been greatly improved, and at the same time, the broad absorption band for TE light becomes more flatter than that in Fig. 6(c) because more electric field is captured by the newly added slit on the graphene. At last, we add the fourth slit on the graphene, as shown in Fig. 6(e), the broadband absorption for TM light is obtained, and the absorption spectral line of both TE and TM light are coincided with each other due to the symmetry of the MA structure. The frequency range with absorption rate over 90% for both TE and TM light is 4.6–8.0 THz, and the absorption bandwidth is as high as 3.4 THz. If we choose 80% absorption rate as the criterion, the absorption frequency range is about 4.2–8.2 THz, and the bandwidth will reach 4 THz. The distribution of the electric field at the two absorption peaks are shown in the inset for TE light, and for TM light, it is exactly the result of TE light rotating 90°. At last, to demonstrate the contribution of the gold disk to the overall absorption, the case where there is no gold disk while four nano-slits are cut out from the graphene disk is simulated. As shown in Fig. 6(f), the broadband absorption is collapsed and the electric field confined on the top layer of the proposed MA also becomes weak, which reveals that the gold disk can indeed enhance the overall absorption performance of the proposed MA structure, and the enhancement of the broadband absorption largely comes from the hybridization and the coupling interaction among the SPRs excited on the gold disk, on the graphene and around the nano-slits in the graphene. Consequently, we choose the combination of gold disk and graphene disk with four symmetrically distributed slits as the top layer of the proposed MA to carry out the following research, and due to its characteristic of rotational symmetry, we only consider the case of TE incident light.

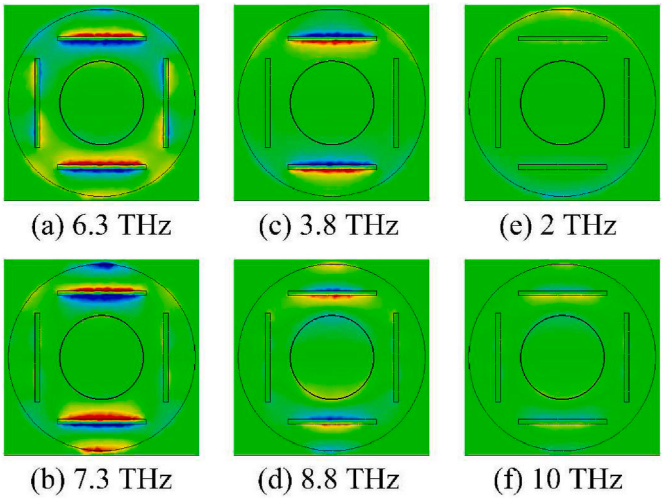

Fig. 7. Distribution of electric field at (a) 6.3 THz and (b) 7.3 THz where the absorption is maximum, at (c) 3.8 THz and (d) 8.8 THz where the absorption is 50%, and at (e) 2 THz and (f) 10 THz which is respectively the lower and upper limits of the considered frequency range.

In order to further understand the physical mechanism of the structure more clearly, as shown in Fig. 7, we plot the electric field distribution of the proposed MA structure shown in Fig. 1(a) at the frequencies of 6.3 THz and 7.3 THz where the absorption rate is maximum, at the frequencies of 3.8 THz and 8.8 THz where the absorption rate is 50%, and at the frequencies of 2 THz and 10 THz which are the upper and lower limits of the considered frequency range. From Fig. 7, we can visually compare the difference in the electric distribution. As shown in Fig. 7(a) at 6.3 THz, (c) at 3.8 THz and (e) at 2 THz, the electric field distribution is mainly concentrated around the upper and lower slits with the field intensity decreasing gradually. The confined electric field is originated from the fundamental SPR along edges of the slit. At the frequency of 6.3 THz, there are some weaker electric fields that are also distributed around the left and right slits on the graphene, which is the higher order SPR and is helpful to enhance the overall absorption. And the electric field on the gold disk is suppressed probably because the out-of-phase distribution of the electric field around the slits and at the edge of the gold disk, which can also be found in terms of

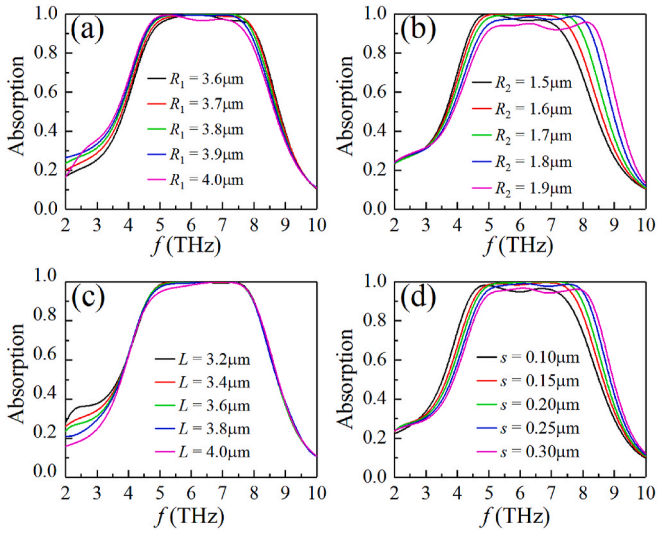

Fig. 8. Absorption spectra as a function of (a) R_1, (b) R_2, (c) L, and (d) s under normally incident TE polarized light, and the other parameters are same as those in Fig. 5.

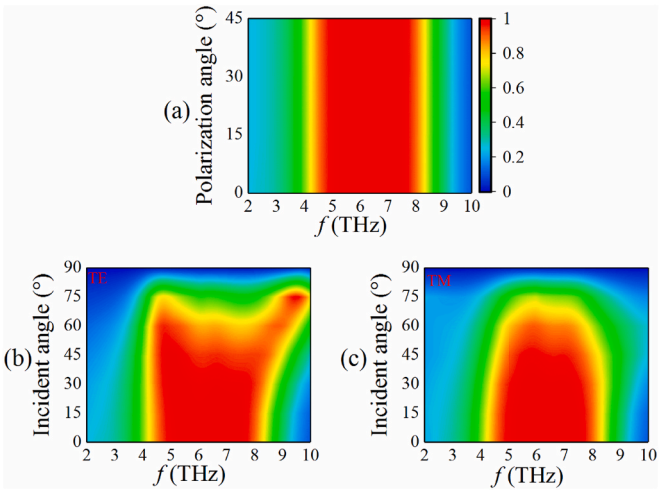

Fig. 9. (a) Absorption spectrum under different polarization angles. Absorption spectrum under different incident angles for (b) TE and (c) TM polarized incident light. The other parameters are same as those in Fig. 5.

Fig. 6(a) and (f). As shown in Fig. 7(b) at 7.3 THz, (d) at 8.8 THz and (f) at 10 THz, the electric field distribution is mainly concentrated at the upper and lower edges of the graphene disk and around the upper and lower slits on graphene with the field intensity decreasing gradually, and the electric field confined around the gold disk is also canceled. In brief, the broadband near perfect absorption mainly comes from three aspects. The first one is the LSPR excited along the edge of the graphene disk and the gold disk, the second one is the LSPR excited around the slits in the graphene, and the third one can be understood as the hybrid interaction among the SPR around the graphene slits, along the edge of gold disk and along the edge of graphene disk.

Taking into account the actual fabrication process and potential tunable ability, the impact of parameter changes on the absorption performance must also be carefully discussed. At first, we discuss the effect of radius of the top graphene disk R_1 on the overall absorption, as shown in Fig. 8(a). It is obvious that the broad absorption band shows a trend of slight redshift when R_1 increases from 3.6μm to 4.0μm, because not only the effective resonant length of LSPR on graphene disk is increased, but also the coupling interaction between the adjacent unit cell will also enhance. At second, the influence of the radius of the gold disk is discussed. It can be found from Fig. 8(b) that when R_2 increases from 1.5μm to 1.9μm, the broad absorption band shows a trend of blueshift and the absorption strength is decreased. Because with the increasing R_2, the hybridization of SPPs between the gold disk and the graphene slits will weaken the overall electric fields confined on the top layer. Therefore, besides the decreased absorption intensity, the total equivalent inductance and capacitance will both decrease, resulting in the blueshift of the absorption band. At the same time, imperfect impedance matching together with the increased ohmic loss will also lead to the decrease of the absorption intensity and the broadening of the absorption band. Next, as shown in Fig. 8(c), it can be clearly seen that the length of the slit L has little influence on the position of the broad absorption band, which can be interpreted through the field distribution shown in Fig. 6(e), and simulations have shown that the field distribution has no clear change when the slit length is slightly changed. But if it is too long, the absorption intensity at low frequency will decrease due to the increasing radiation loss, so we choose $L = 3.6\mu$m as the optimal value in this paper. At last, as shown in Fig. 8(d), it is obvious that the width of the slits have more effects on the absorption property than it length. With the increase of slit width, the broad absorption band will have an obvious blueshift, and the absorption intensity will also decrease. The physical reason can also be found in terms of the field distribution shown in Fig. 6(e). Simulation results have shown that with the increase of the width of nano-slits, the electric field confined on the top layer, especially around the nano-slits at high frequency, will become weak gradually. As a result, the induced capacitance and inductance will also decrease, leading to the blueshift of the absorption band. Meanwhile, the weakened resonance together with the impedance mismatch lead to the reduction of the absorption intensity. In brief, some slight changes of the geometry parameters will not have remarkable effect on the overall broadband absorption characteristics of the proposed MA, which means the bigger tolerance in real fabricating.

As mentioned above, the MA proposed in this work will be independent of the polarization direction of the normally incident light because it is rotational symmetric, which can be further verified, as simulated in Fig. 9(a). In addition, for a wider range of application fields, the absorption performance under variable incident angles is also needed to be discussed with the optimal structure parameters mentioned above. The absorption spectra with different incident angles for TE and TM polarized wave are shown in Fig. 9(b) and (c). For TE light, one can find that the broad absorption band can be maintained at a high level when the incident angle increases from 0° to55°. When the incident angles continue to increase to larger than 55°, the high frequency side of the broad absorption band will exhibit a trend of blueshift, and the broad absorption band begins to collapse rapidly when the incident angle is further increased. This is because that as the incident angle continue to increase, the incident light will gradually become grazing incidence, resulting in the decrease of the interaction between the incident light and the proposed MA. As a result, the LSPR excited on the top layer of the proposed MA can no longer be maintained at the stronger states, and at the same time, the parasitic resonance and the diffraction will also increase, which are all the reasons for the change of the absorption performance shown in Fig. 9(b). As for the TM case shown in Fig. 9(c), the broad absorption band will keep stable when the incident angle is below 45°. As the incident angles continue to increase, the broad absorption band will become narrower together with the decline of the absorption intensity. It is worth nothing that the absorption rate can be maintained at a higher value when the incident angle is below 60°, and it will drop sharply when the incident angle is larger than 70°. This is because that with the increase of incident angles, the electric field energy projected onto the top layer of the proposed MA will decrease gradually. When the incident angle is too large, the electric field is not strong enough to excite SPP on the top layer of the MA structure, so the absorption will decrease rapidly. Nevertheless, the range of incident angles is still relatively wide, therefore, the excellent absorption

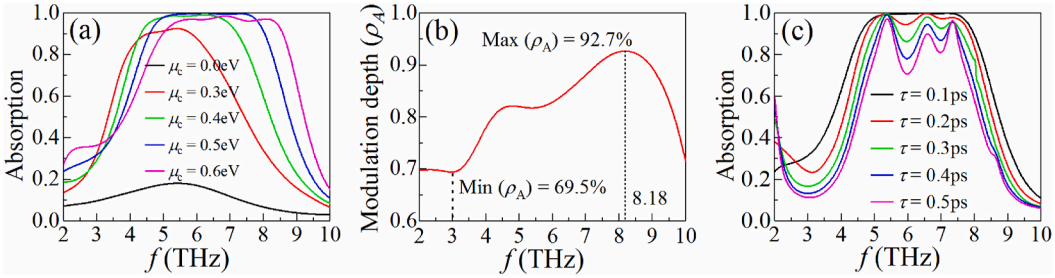

Fig. 10. (a) Absorbance spectra under different chemical potentials μ_c, (b) modulation depth when μ_c is switched from 0 eV to 0.5 eV, and (c) absorbance spectra under different relaxation time τ.

characteristic of wide incident angles and polarization insensitivity will make the proposed MA have potential application values in many areas, such as energy harvest, high speed communication, information storage, stealth materials and so on.

One of the reasons why graphene is widely used in various metamaterial devices is that its conductivity can be adjusted dynamically through changing the chemical potential by different methods. Therefore, we next study the dynamically tunable broadband absorption characteristics of the proposed MA structure by adjusting the chemical potential of graphene from 0 eV to 0.6 eV, and the simulation result is shown in Fig. 10(a). It can be clearly seen that when the chemical potential of graphene is 0 eV, the absorption spectrum of the proposed MA structure for TE incident light is less than 20%. But as the chemical potential continues to increase from 0.3 eV to 0.6 eV, together with the blueshift of the absorption spectrum, the broadband absorption characteristic is exhibited with the intensity of the broad absorption band gradually increasing to larger than 90%. When the chemical potential is 0.5 eV, nearly perfect broadband absorption is achieved due to the perfect impedance matching between the MA and the free space. Considering a potential application, taking use of the absorption characteristic under 0 eV and 0.5 eV, the proposed MA can be used as a THz switch or a THz modulator. Since the maximum absorption rate is less than 20% when the chemical potential of graphene is 0 eV, therefore, it can be regarded as the off-state. On the contrary, the absorption rate is close to 100% when the chemical potential of graphene is 0.5 eV and it can be referred to as the on-state. As a result, we can obtain better switching characteristics within a broad frequency range from 4.6 THz to 8 THz through switching the chemical potential between 0 eV and 0.5 eV under the controlling of external gate voltage. Meanwhile, as a modulator, the modulation depth (MD) can be defined as $\rho_A = (A_{on} - A_{off})/A_{on}$, where A_{on} and A_{off} are respectively the absorption of on-state and off-state. The calculated absorption MD is shown in Fig. 10(b). It can be found that the minimum absorption MD is about 69.5% at 3 THz and the maximum absorption MD is about 92.7% at 8.18 THz. Therefore, the proposed MA structure indeed demonstrates good modulation characteristic for the incident light, which have potentials in many dynamically tunable THz metamaterial devices not limited to MAs. In fact, it is well-known that weak absorption means strong reflection and vice versa. Therefore, when the chemical potential is 0 eV, the proposed metamaterial device can act as a THz reflector, which is also a potential application aspect. To be noted is that, in terms of the above mentioned relationship between the graphene chemical potentials and the gate voltages, the required gate voltage corresponding to the considered graphene chemical potentials of 0 eV, 0.3 eV, 0.4 eV, 0.5 eV, and 0.6 eV can be calculated as 0 V, 0.4 V, 0.77 V, 1.2 V, and 1.73 V, respectively, which is easy to be manipulated in practical experiments. Simulation result shown in Fig. 10(c) is the absorption spectra under different graphene relaxation time. It is obvious that as the relaxation time increases from 0.1 ps to 0.2 ps, the flat broad absorption band begins to fluctuate. And when the relaxation time is increased to $\tau = 0.5$ ps, three absorption peaks occur in the broad absorption band, indicating a trend of transition from broadband absorption to multiband absorption. The reason why the proposed MA structure can achieve broadband absorption with higher absorption intensity at relaxation time $\tau = 0.1$ ps and $\mu_c = 0.5$ eV is that the carrier concentration relative to the plasmonic oscillation approaches saturation at this time and under the overall parameter conditions mentioned in this paper. When the graphene relaxation time is changed, a part of the energy will be reflected, resulting in a decrease in the absorption intensity together with the narrower absorption band.

To further increase the absorption band of the proposed MA structure, one method is to increase the number of functional layers, and the other one is to change the pattern shape of the current resonant layer on top of the Topas layer to generate more resonant effect. Here, as an exploratory research, the second method is chosen to increase the absorption bandwidth. It is worth nothing that both of the two methods will increase the difficulty of fabrication, but it is also achievable by the state-of-art fabrication technology. Inspired by the aforementioned research result, it is known that the use of gold disk together with the graphene pattern beneath the gold disk can effectively and efficiently

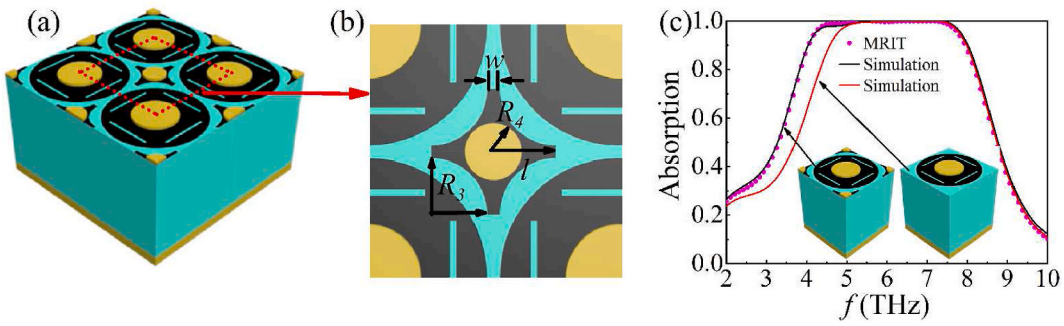

Fig. 11. (a) Schematic diagram of the newly designed MA structure, (b) top view of a unit cell of the newly designed MA structure, and (c) comparison of the absorption spectra between the two MA structures, the black solid curve and the pink dotted curve are simulated result and the MRIT result for the newly designed MA structure, respectively, while the red solid curve is the simulated result of the MA structure shown in Fig. 1.)

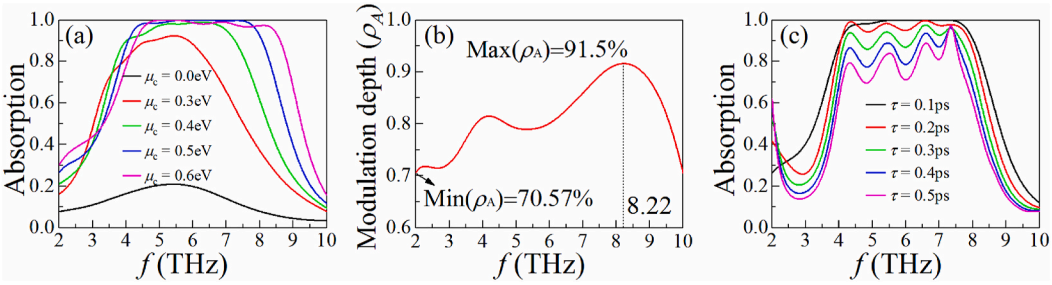

Fig. 12. (a) Absorbance spectra under different chemical potentials μ_c for the newly designed MA structure, (b) modulation depth when μ_c is switched from 0 eV to 0.5 eV, and (c) absorbance spectra under different relaxation time τ.

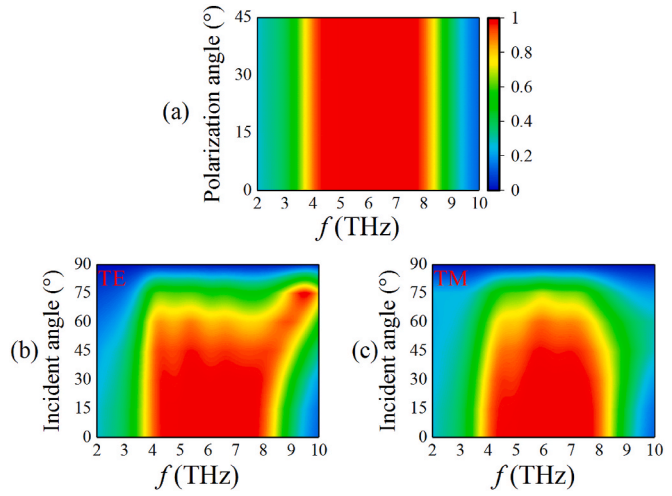

Fig. 13. (a) Absorbance spectrum under different polarization angle, (b) Absorbance spectrum with different incident angle under normal TE wave, (c) Absorbance spectrum with different incident angle under normal TM wave.

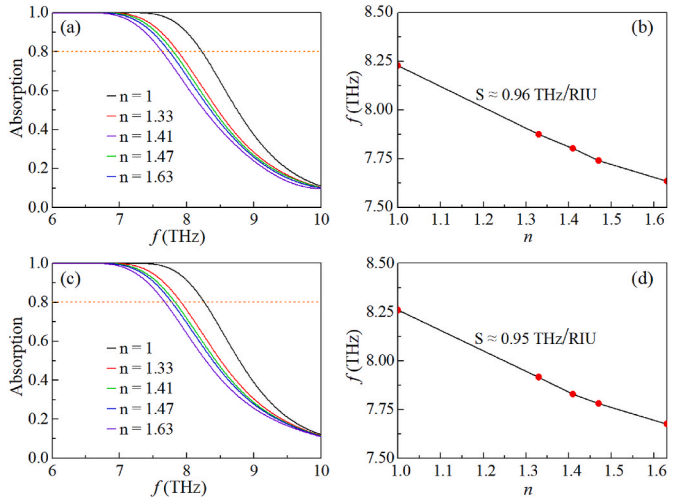

Fig. 14. (a) Absorption spectra as a function of refractive index when the samples to be detected are coated on the top of the MA structure shown in Fig. 1, and (b) dependence of the frequency on the refractive index n of the sample to be detected when the absorption is 80%. (c) and (d) are the same results for the MA structure shown in Fig. 11.

enhance the overall absorption performance. Therefore, we try to add a new combination of gold disk and graphene pattern into the proposed MA structure, and the newly designed MA structure is shown in Fig. 11 (a). The graphene pattern is formed by cutting off four quarter circles with radius R_3 from a square graphene patch with side length $2l$, where $l = P/4$. The radius of the newly added gold disk is $R_4 = R_3/2$, it is on the top of the graphene pattern, as shown in Fig. 11(b). Other parameters are the same as those mentioned above except for $R_3 = 1.8\mu$m. It can be found from Fig. 11(c) that the absorption bandwidth is indeed broadened from 4.6–8 THz to about 4–8 THz compared with the original MA structure. The result calculated by MRIT (pink dotted curve) also agrees well with the simulation result.

The tunable broadband absorber performance of the newly designed MA structure is also discussed. As the chemical potential of graphene changes from 0 eV to 0.6 eV, the change trend of the absorption band is similar to that mentioned in Fig. 10, namely, the absorption bandwidth will broaden with the increase of graphene chemical potential, as shown in Fig. 12(a). Meanwhile, it can be seen from Fig. 12(b) that the newly designed MA structure still has excellent modulation characteristics, of which the maximum and minimum modulation depth (MD) is 91.5% and 70.57%, respectively. Furthermore, increasing the relaxation time of graphene from 0.1 ps to 0.5 ps will also lead to the deterioration of the broadband absorption characteristics, resulting in the fluctuation of the flat absorption band and the decrease of the overall absorption intensity, as shown in Fig. 12(c).

It is worth nothing that the newly designed MA structure is still a rotational symmetric structure, therefore, it also has the characteristic of polarization insensitive, which can be verified from Fig. 13(a). The influence of the incident angle on its absorption characteristics for TE and TM incident light is shown in Fig. 13(b) and (c) respectively. It can be clearly seen that when the incident angle is below 45°, the absorption bandwidth can still keep unchanged for both TE and TM incident light, which is also similar to those shown in Fig. 9.

Furthermore, considering one of the potential applications of the proposed MA structures, we also simulated the sensing performances. The samples to be detected and their refractive indices are selected as water ($n = 1.33$), ethylene glycol ($n = 1.41$), glycerin ($n = 1.47$), and carbon disulfide ($n = 1.63$). During simulation, samples with thickness of 3μm are covered on top of the proposed MA structures and the sensitivity is defined as $S = \Delta f/\Delta n$, which shows the change of frequencies resulted from the change of refractive index. For the MA structure shown in Fig. 1, as shown in Fig. 14(a), it is obvious that the absorption spectra will redshift with the increase of the sample's refractive index. For simplicity, we only draw the transmission spectra of the high-frequency side, and there is a similar trend on the low-frequency side. The clear redshift of the absorption spectra indicates that the absorption performance of the proposed MA is sensitive to the refractive index of the covered sample, which shows the possible application of refractive index sensing to measure the refractive index of the sample to be detected which is covered onto the MA structure. The calculated result shown in Fig. 14(b) demonstrates that when we select 80% as the absorption intensity, the corresponding frequency will change linearly with the increase of the refractive index of the samples. Meanwhile, the calculated sensitivity is up to about 0.96THz/RIU, which is high enough for the potential application [60]. Then the sensing property of the structure shown in Fig. 11 is also studied, and the

Table 1
Comparison with some reported literatures.

References	Absorption frequency band when		RAB when		Thickness (μm)	Maximum MD	S (THz/RIU)
	A>90%	A>97%	A = 90%	A = 97%			
[21]	0.39–0.72 THz	0.43–0.68 THz	60%	45%	70.5	–	–
[36]	1.27–2.59 THz	2.0–2.45 THz	68%	20%	26.5	–	–
[37]	1.48–2.79 THz	1.75–2.59 THz	61%	39%	27.04	84.8%	–
[38]	1.05–2.35 THz	1.15–1.42 THz	76%	21%	24.8	–	–
[40]	1.38–3.4 THz	2.9–3.3 THz	84.5%	13%	21.5	–	–
This work (Fig. 1)	4.6–8.0 THz	4.9–7.7 THz	54%	44%	8.4	92.7%	0.96
This work (Fig. 11)	4.0–8.0 THz	4.4–7.8 THz	67%	56%	8.4	91.5%	0.95

results are shown in Fig. 14(c) and (d), which show similar phenomena as those shown in Fig. 14(a) and (b).

Finally, comparison between the results of the proposed absorber structure and some recently published works presented in the field of broadband absorbers are summarized in Table 1, where the absorption bandwidth with absorption coefficient larger than 90% and 97%, the relative absorption bandwidth (RAB) when the absorption coefficients are respectively 90% and 97%, the overall thickness of the studied metamaterial absorbers, maximum modulation depth (MD), and sensitivity as a refractive sensor (S) are demonstrated. It is clear that the proposed structure not only has more compact structure size, wider absorption band and more advantageous RAB simultaneously, but also has larger MD and acceptable sensitivity, which makes the proposed metamaterial absorber have more potential application values in sub-wavelength optoelectronic devices.

4. Conclusion

In conclusion, we have proposed a broadband MA containing both graphene pattern and gold disk, which can realize broadband absorption characteristics with the bandwidth as wide as 3.4 THz. By adding a new combination of graphene pattern and gold disk to the same layer of the MA structure, the newly designed MA structure can achieve wider absorption bandwidth. Compared with the initially proposed MA structure, the bandwidth of the newly designed MA structure is up to 4 THz. At the same time, both of the two MA structures have better modulation characteristics of the maximum/minimum modulation depth 92.7%/69.5% and 91.5%/70.57% when the chemical potential of graphene is switched from 0 eV to 0.5 eV. Meanwhile, both of the two MA structures have the absorption characteristics of dynamically tunable, polarization insensitive and wide angle incidence. In addition, the proposed MA structures also shows the good property for the potential application of THz modulator, THz switch and THz refractive index sensing. Therefore, the MA proposed in this paper will have great potential application value in energy absorbers, high speed intelligent detection devices, modulators, and optoelectronics in THz frequency range.

Declaration of competing interest

The authors declare that they have no known competing financial interests or personal relationships that could have appeared to influence the work reported in this paper.

Acknowledgement

This work was supported by the National Natural Science Foundation of China (Grants No. 61775126).

References

[1] R.A. Shelby, D.R. Smith, S. Schultz, Experimental verification of a negative index of refraction, Science 292 (5514) (2001) 77–79.
[2] D.R. Smith, W.J. Padilla, D.C. Vier, S.C. Nemat-Nasser, S. Schultz, Composite medium with simultaneously negative permeability, Phys. Rev. Lett. 84 (18) (2000) 4184–4187.
[3] F. Alves, D. Grbovic, B. Kearney, N.V. Lavrik, G. Karunasiri, Bi-material terahertz sensors using metamaterial structures, Opt Express 21 (11) (2013) 13256–13271.
[4] J. Liu, L. Fan, J. Ku, L. Mao, Absorber: a novel terahertz sensor in the application of substance identification, Opt. Quant. Electron. 48 (2) (2016) 80.
[5] M. Mittendorff, S. Winnerl, J. Kamann, J. Eroms, D. Weiss, H. Schneider, M. Helm, Ultrafast graphene-based broadband THz detector, Appl. Phys. Lett. 103 (2) (2013) 21113.
[6] J.B. Pendry, Negative refraction makes a perfect lens, Phys. Rev. Lett. 85 (18) (2000) 3966–3969.
[7] N. Fang, H. Lee, C. Sun, X. Zhang, Sub-diffraction-limited optical imaging with a silver superlens, Science 308 (5721) (2005) 534–537.
[8] W. Zhu, Y. Huang, I.D. Rukhlenko, G. Wen, M. Premaratne, Configurable metamaterial absorber with pseudo wideband spectrum, Opt Express 20 (6) (2012) 6616–6621.
[9] H. Xiong, J.S. Hong, C.M. Luo, L.L. Zhong, An ultrathin and broadband metamaterial absorber using multi-layer structures, J. Appl. Phys. 114 (6) (2013) 64109.
[10] B. Wu, H.M. Tuncer, M. Naeem, B. Yang, M.T. Cole, W.I. Milne, Y. Hao, Experimental demonstration of a transparent graphene millimeter wave absorber with 28% fractional bandwidth at 140 GHz, Sci. Rep. 4 (2014) 4130.
[11] A. Fardoost, F.G. Vanani, A.a. Amirhosseini, R. Safian, Design of a multilayer graphene-based ultrawideband terahertz absorber, IEEE Trans. Nanotechnol. 16 (1) (2017) 68–74.
[12] Y. Gao, I.V. Shadrivov, Second harmonic generation in graphene-coated nanowires, Opt. Lett. 41 (15) (2016) 3623–3626.
[13] W.L. Guo, Y.X. Liu, T.C. Han, Ultra-broadband infrared metasurface absorber, Opt Express 24 (18) (2016) 20586–20592.
[14] H. Tao, N.I. Landy, C.M. Bingham, X. Zhang, R.D. Averitt, W.J. Padilla, A metamaterial absorber for the terahertz regime: design, fabrication and characterization, Opt Express 16 (10) (2008) 7181–7188.
[15] L. Huang, H. Chen, Multi-band and polarization insensitive metamaterial absorber, Prog. Electromag. Res. 113 (2011) 103–110.
[16] Q.W. Ye, Y. Liu, H. Lin, M.H. Li, H.L. Yang, Multi-band metamaterial absorber made of multi-gap SRRs structure, Appl. Phys. A 107 (2012) 155–160.
[17] J.W. Park, P.V. Tuong, J.Y. Rhee, K.W. Kim, W.H. Jang, E.H. Choi, L.Y. Chen, Y. P. Lee, Multi-band metamaterial absorber based on the arrangement of donut-type resonators, Opt Express 21 (8) (2013) 9691.
[18] F.R. Hu, L. Wang, B.G. Quan, X.L. Xu, Z. Li, Z.A. Wu, X.C. Pan, Design of a polarization insensitive multiband terahertz metamaterial absorber, J. Phys. D Appl. Phys. 46 (8) (2013), 195103.
[19] G.Q. Liu, Y. Liu, X.S. Liu, J. Chen, G.L. Fu, Z.Q. Liu, Large-area, low-cost, ultra-broadband, infrared perfect absorbers by coupled plasmonic-photonic micro-cavities, Sol. Energy Mater. Sol. Cell. 186 (2018) 142–148.
[20] Y. Zhou, Z. Qin, Z.Z. Liang, D.J. Meng, H.Y. Xu, D.R. Smith, Y.C. Liu, Ultra-broadband metamaterial absorbers from long to very long infrared regime, Light Sci. Appl. 10 (2021) 138.
[21] Z.Y. Song, K. Wang, J. Li, Q.H. Liu, Broadband tunable terahertz absorber based on vanadium dioxide metamaterials, Opt Express 26 (6) (2018) 7148.
[22] S.T. Song, F.Y. Liu, L.M. Qi, Z. Zhang, H.D. Wang, Y.T. Zhou, A MoS2-based broadband and multiband metamaterial absorber in the visible band, Mod. Phys. Lett. B 34 (2020), 2050397.
[23] Y.M. Qing, H.F. Ma, T.J. Cui, Tailoring anisotropic perfect absorption in monolayer black phosphorus by critical coupling at terahertz frequencies, Opt Express 26 (25) (2018) 32442.
[24] A.H. Castro Neto, F. Guinea, N.M.R. Peres, K.S. Novoselov, A.K. Geim, The electronic properties of graphene, Rev. Mod. Phys. 81 (2009) 109–162.
[25] R.R. Nair, P. Blake, A.N. Grigorenko, K.S. Novoselov, T.J. Booth, T. Stauber, N.M. R. Peres, A.K. Geim, Fine structure constant defines visual transparency of graphene, Science 320 (2008) 1308.
[26] R. Alaee, M. Farhat, C. Rockstuhl, F. Lederer, A perfect absorber made of a graphene micro-ribbon metamaterial, Opt Express 20 (27) (2012) 28018.
[27] S. Barzegar-Parizi, Graphene-based tunable dual-band absorbers by ribbon/disk array, Opt. Quant. Electron. 51 (2019) 167.
[28] J.G. Zhang, J.P. Tian, L. Li, A dual-band tunable metamaterial near-unity absorber composed of periodic cross and disk graphene arrays, IEEE Photonics J. 10 (2) (2018), 4800512.
[29] J. Wu, Tunable multi-band terahertz absorber based on graphene nano-ribbon metamaterial, Phys. Lett. 383 (22) (2019) 2589–2593.

[30] L.Y. Jiang, C. Yuan, Z.Y. Li, J. Su, Z. Yi, W.T. Yao, P.H. Wu, Z.M. Liu, S.B. Cheng, M. Pan, Multi-band and high-sensitivity perfect absorber based on monolayer graphene metamaterial, Diam. Relat. Mater. 111 (2021), 108227.
[31] K.D. Xu, Y. Cai, X.B. Cao, Y.J. Guo, Y.L. Zhang, Q. Chen, Multi-band THz absorbers using T-shaped slot-patterned graphene and its complementary structure, J. Opt. Soc. Am. B 37 (10) (2020) 3034–3040.
[32] R.J. Ke, J.P. Tian, R.C. Yang, W.H. Pei, Dual-band tunable perfect absorber based on monolayer graphene pattern, Result. Phys. 18 (2020), 103306.
[33] M. Pan, H.Z. Huang, B.D. Fan, W.Z. Chen, S. Li, Q.L. Xie, F. Xu, D.W. Wei, J. Fang, Theoretical design of a triple-band perfect metamaterial absorber based on graphene with wide-angle insensitivity, Result. Phys. 23 (2021), 104037.
[34] X.S. Liu, G.Q. Liu, P. Tang, G.L. Fu, G.Z. Du, Q.Q. Chen, Z.Q. Liu, Quantitatively optical and electrical-adjusting high-performance switch by graphene plasmonic perfect absorbers, Carbon 140 (2018) 362–367.
[35] M. Amin, M. Farhat, H. Bagcı, An ultra-broadband multilayered graphene absorber, Opt Express 21 (24) (2013) 29938.
[36] L.F. Ye, Y. Chen, G.X. Cai, N. Liu, J.F. Zhu, Z.Y. Song, Q.H. Liu, Broadband absorber with periodically sinusoidally-patterned graphene layer in terahertz range, Opt Express 25 (10) (2017) 11223.
[37] L.F. Ye, X.E. Chen, C.H. Zhu, W.W. Li, Y. Zhang, Switchable broadband terahertz spatial modulators based on patterned graphene and vanadium dioxide, Opt Express 28 (23) (2020) 33948.
[38] M. Zhang, Z.Y. Song, Terahertz bifunctional absorber based on a graphene-spacer-vanadium dioxide-spacer-metal configuration, Opt Express 28 (8) (2020) 11780.
[39] P.D. Cunningham, N.N. Valdes, F.A. Vallejo, L.M. Hayden, B. Polishak, X.H. Zhou, J.D. Luo, A.K.-Y. Jen, J.C. Williams, R.J. Twieg, Broadband terahertz characterization of the refractive index and absorption of some important polymeric and organic electro-optic materials, J. Appl. Phys. 109 (2011) 43505.
[40] L.F. Ye, X. Chen, G.X. Cai, J.F. Zhu, N. Liu, Q.H. Liu, Electrically tunable broadband terahertz absorption with hybrid-patterned graphene metasurfaces, Nanomaterials 8 (8) (2018) 562.
[41] J.S. Li, D.X. Yan, J.Z. Sun, Flexible dual-band all-graphene-dielectric terahertz absorber, Opt. Mater. Express 9 (5) (2019) 2067–2075.
[42] M.H. Dinh, M.T. Le, S.T. Ngo, T.V. Huynh, N.T. Tung, Terahertz cut-wire-pair metamaterial absorber, J. Appl. Phys. 130 (2021) 13102.
[43] J. Ma, Y.J. Huang, M.B. Pu, D. Xu, J. Luo, Y.H. Guo, X.G. Luo, Inverse design of broadband metasurface absorber based on convolutional autoencoder network and inverse design network, J. Phys. D Appl. Phys. 53 (2020), 464002.
[44] G. Jo, M. Choe, C.Y. Cho, J.H. Kim, W. Park, S. Lee, W.K. Hong, T.W. Kim, S. J. Park, B.H. Hong, Large-scale patterned multi-layer graphene films as transparent conducting electrodes for GaN light-emitting diodes, Nanotechnology 21 (17) (2010), 175201.
[45] Z.Y. Fang, Y.M. Wang, A.E. Schlather, Z. Liu, P.M. Ajayan, F.J.G. de Abajo, P. Nordlander, Z. Zhu, N.J. Halas, Active tunable absorption enhancement with graphene nanodisk arrays, Nano Lett. 14 (1) (2014) 299–304.
[46] Q.Q. Zhuo, Q. Wang, Y.P. Zhang, D. Zhang, Q.L. Li, C.H. Gao, Y.Q. Sun, L. Ding, Q. J. Sun, S.D. Wang, J. Zhong, X.H. Sun, S.T. Lee, Transfer-free synthesis of doped and patterned graphene films, ACS Nano 9 (1) (2015) 594–601.
[47] L.Z. Wang, J. Zhang, N. Liu, Y.K. Wang, P.A. Hu, Z.L. Wang, Fast patterned graphene ribbons via soft–lithography, Procedia CIRP 42 (2016) 428–432.
[48] G.W. Hanson, Dyadic Green's functions and guided surface waves for a surface conductivity model of graphene, J. Appl. Phys. 103 (6) (2008) 64302.
[49] A. Vakil, N. Engheta, Transformation optics using graphene, Science 332 (2011) 1291.
[50] F. Zeng, L.F. Ye, L. Li, Z.H. Wang, W. Zhao, Y. Zhang, Tunable mid-infrared dual-band and broadband cross-polarization converters based on U-shaped graphene metamaterials, Opt Express 27 (23) (2019) 33826–33839.
[51] Z.Y. Fang, Y.M. Wang, A.E. Schlather, Z. Liu, P.M. Ajavan, F. Javier Garcia de Abajo, P. Nordlander, X. Zhu, N.J. Halas, Active tunable absorption enhancement with graphene nanodisk arrays, Nano Lett. 14 (2014) 299–304.
[52] V. Thareja, J.H. Kang, H.T. Yuan, K.M. Milaninia, H.Y. Hwang, Y. Cui, P.G. Kik, M. L. Brongersma, Electrically tunable coherent optical absorption in graphene with ion gel, Nano Lett. 15 (2015) 1570–1576.
[53] Z.Q. Miao, Q. Wu, X. Li, Q. He, K. Ding, Z.H. An, Y.B. Zhang, L. Zhou, Widely tunable terahertz phase modulation with Gate-Controlled graphene metasurfaces, Phys. Rev. X 5 (2015) 41027.
[54] C.F. Chen, C.H. Park, B.W. Boudouris, J. Horng, B.S. Geng, C. Girit, A. Zettl, M. F. Crommie, R.A. Segalman, S.G. Louie, F. Wang, Controlling inelastic light scattering quantum pathways in graphene, Nature 471 (2011) 617–620.
[55] D. Hu, T.H. Meng, H.Y. Wang, Y.K. Ma, Tunable broadband terahertz absorber based on plasmon hybridization in monolayer graphene ring arrays, Appl. Opt. 59 (35) (2020) 11053–11058.
[56] H.T. Chen, Interference theory of metamaterial perfect absorbers, Opt Express 20 (7) (2012) 7165–7172.
[57] D.R. Smith, S. Schultz, P. Markos, C.M. Soukoulis, Determination of negative permittivity and permeability of metamaterials from reflection and transmission coefficients, Phys. Rev. B. 65 (2002), 195104.
[58] L.H. Christopher, F.K. Edward, Andrew dienstfrey. "Characterizing metasurfaces/metafilms: the connection between surface susceptibilities and effective material properties", IEEE Antenn. Wireless Propag. Lett. 10 (2011) 1507–1511.
[59] D.R. Smith, D.C. Vier, T. Koschny, C.M. Soukoulis, Electromagnetic parameter retrieval from inhomogeneous metamaterials, Adv. Opt. Mater. 71 (2005) 36617.
[60] Y.P. Qi, Y. Zhang, C.Q. Liu, T. Zhang, B. Zhang, L.Y. Wang, et al., A tunable terahertz metamaterial absorber composed of elliptical ring graphene arrays with refractive index sensing application, Result. Phys. 16 (2020), 103012.